Corrosion Science 190 (2021) 109663

Contents lists available at ScienceDirect

Corrosion Science

journal homepage: www.elsevier.com/locate/corsci

Remarkable cavitation erosion–corrosion resistance of CoCrFeNiTiMo high-entropy alloy coatings

Jiang Xu [a,*], Shuang Peng [a], Zhengyang Li [b], Shuyun Jiang [c], Zong-Han Xie [d], Paul Munroe [e], Hong Lu [f]

[a] Department of Material Science and Engineering, Nanjing University of Aeronautics and Astronautics, 29 Yudao Street, Nanjing, 210016, PR China
[b] Institute of Mechanics, Chinese Academy of Sciences, Beijing, 100190, PR China
[c] Department of Mechanical Engineering, Southeast University, 2 Si Pai Lou, Nanjing, 210096, PR China
[d] School of Mechanical Engineering, University of Adelaide, SA, 5005, Australia
[e] School of Materials Science and Engineering, University of New South Wales, NSW, 2052, Australia
[f] Xin Jiang Yihe Biology Co., Ltd, Regiment Headquarters of Crops 66, Cocodala, 835219, PR China

ARTICLE INFO

Keywords:
High entropy alloy coating
Cavitation erosion
Potentiodynamic polarization
Electrochemical impedance spectroscopy

ABSTRACT

A CoCrFeNiTiMo high entropy alloy (HEA) coating was prepared onto a Ti-6Al-4 V substrate using the double cathode glow discharge method. This innovative HEA coating exhibited a duplex phase microstructure, composed of a BCC-structure solid solution phase and a tetragonal structured intermetallic phase, Co_2Mo_3, and possessed high hardness, high load bearing capacity and strong adhesion to the substrate. The HEA coating underwent much less severe cavitation erosion damage in a 3.5 % NaCl solution relative to Ti-6Al-4 V according to the results of electrochemical measurements and the cumulative weight loss, because of its unique combination of excellent mechanical properties and high corrosion resistance.

1. Introduction

In general, most traditional metallic materials, including ferrous-, aluminum-, copper-, magnesium- and titanium-based alloys, are typically based on a single phase or duplex matrix, to which small amounts of other elements are incorporated to improve its properties. The main problem of this design strategy lies in a restrictive use of principal elements in an attempt to avoid the formation of complex intermetallic compounds that would compromise the mechanical properties of metallic alloys. More than ten years ago, a newly developed category of multi-component alloys, also termed high-entropy alloys (HEAs), broke through the bottleneck of conventional alloy design and facilitated the exploration of a vast array of alloy compositions. Such alloys normally consist of at least five elements in near equiatomic ratios with the atomic concentration for each element varying between 5 at.% and 35 at.% [1,2]. Owing to their high configurational entropy and sluggish diffusion, the HEAs tend to form as simple crystal structured solid-solution phases, such as body-centered cubic (BCC), face-centered cubic (FCC), or hexagonal close-packed (HCP) [3,4]. Through a combination of their structure and composition, HEAs possess many exciting properties differing from conventional alloys, such as excellent mechanical properties over a wide temperature range, superior resistance to corrosion and high-temperature oxidation, good electrical and magnetic properties, and so show great potential for a wide range of engineering applications as both structural and functional materials [5–7].

Currently, the most common HEAs are made of transition metal elements, such as Fe, Ni, Co and Cr, mixed with other alloying elements Al, Mn, Mo, V and Ti to further unite the strength and ductility in alloys [8,9]. However, relatively low strength and wear resistance have hindered their broader industrial application. Various strategies have been pursued to overcome those drawbacks through both solid solution alloying and second phase reinforcement. For instance, Rubio et al. [10] investigated the influence of Mo and Ti additions on the microstructural evolution and mechanical properties of AlCoFeNi HEAs. They found that under sintered states, adding Mo and Ti elements raised the microhardness values of the alloys from 556 $HV_{0.2}$ to 639 $HV_{0.2}$ and 681 $HV_{0.2}$, respectively, and the hardness value was further increased to 894 $HV_{0.2}$ via the combined addition of Mo and Ti. Guo et al. [11] investigated the mechanical and tribological properties CoCrFeNiMn HEA matrix composites prepared by spark plasma sintering. The results indicated that the addition of 10 % Cr_3C_2 to a CoCrFeNiMn-based HEA generated a composite with excellent yield strength and wear resistance.

* Corresponding author.
E-mail address: xujiang73@nuaa.edu.cn (J. Xu).

https://doi.org/10.1016/j.corsci.2021.109663
Received 7 April 2021; Received in revised form 4 June 2021; Accepted 2 July 2021
Available online 5 July 2021

Since these HEAs often contain expensive alloying elements, they are particularly attractive for application as a surface coating material for economic reasons. In addition, although an extensive effort has been made toward the understanding of the mechanical or corrosion behavior of HEAs, little work has been done to explore the response of HEAs to simultaneous mechanical and electrochemical actions. Some engineering components used in high speed fluid flow systems, such as hydropower turbines, water pumps and ship propellers, often suffer from severe cavitation erosion–corrosion attack [12,13]. Under these circumstances, as the pressure in the liquid is above the vapor pressure, micron-size vapor bubbles inside the liquid flow implode violently, leading to the impingement of high velocity microjets with a transient pressure reaching several GPa and a velocity of several hundred meters per second [14]. The solid surfaces subjected to the repetitive attacks of impact loading undergo intense plastic deformation, hence crack initiation and propagation, and eventually material surface destruction [15]. This localized mechanical damage is intensified by the presence of an aggressive species in corrosive media, where the cavitation degradation mechanism works together with the corrosion process. The mutual reinforcement of cavitation erosion and corrosion is reflected as: (1) erosion-enhanced corrosion, where the mechanical shock can disrupt surface passive films developed on the components, thus exposing unprotective fresh surfaces to the corrosive environment so speeding up the corrosion process [16]; (2) corrosion-enhanced erosion, where localized corrosion processes not only induce the degradation of mechanical properties, but also act to roughen material surfaces, thereby enhancing the erosion rate [17]. The interactions of these two factors enable the total weight loss to be larger than the summation of pure cavitation erosion and corrosion, as separate phenomena.

The cavitation erosion–corrosion property of a material not only depends on the aggressiveness of the medium, such as pH value, the intensity of cavitation and solution temperature, but it is also closely linked to mechanical property and corrosion resistance of the material under operation conditions. Considering that the cavitation erosion–corrosion is a phenomenon directly associated with surface degradation, hard coatings are often used to protect metal components in service. Among a variety of surface treatment techniques, double-cathode glow discharge process has shown promise to enhance the surface properties of metal substrates, such as 316 l stainless steel and Ti-6Al-4 V, through the deposition of nanoscale metal silicide or nitride coatings [18,19]. Moreover, in view of the appealing mechanical properties and electrochemical stability of HEAs, an emerging trend has risen to exploit the application of HEAs as cavitation erosion resistant coatings. For example, Zhang et al. reported the fabrication of the FeCoCrAlNi HEA coating on a 304 stainless steel substrate by laser surface alloying and investigated the cavitation erosion behavior of this coating in 3.5 %NaCl solution [20]. The results showed that the cavitation erosion resistance of 304 stainless steel increased by 7.6 times after coated with the HEA, which imparted an excellent combination of toughness and hardness.

In this study, the cavitation erosion–corrosion behavior of a CoCrFeNiTiMo HEA coating, prepared by a double cathode glow discharge technique, was systematically studied by ultrasonic cavitation erosion testing in a 3.5 wt% NaCl solution. To reveal the corresponding mechanism of cavitation erosion–corrosion, the surface morphologies of eroded coatings, constituents of the passive films and weight loss analysis were investigated.

2. Experimental details

2.1. Coatings preparation

The HEA coating was deposited on to Ti-6Al-4 V substrate using a double-cathode glow discharge system. The substrates were prepared from a rod of commercially sourced Ti-6Al-4 V. They were then mirror polished using, first, SiC abrasive papers and then, a 0.5 μm Cr_2O_3 powder colloidal solution. As a final step samples were cleaned in acetone and blown dried. An equimolar CoCrFeNiTiMo HEA target, which acted as one of the cathodes, was prepared from 99.99 % purity elemental powders. These were pressed into a target via cold compaction with an applied force of 600 MPa. Deposition using the double-cathode glow discharge system occurred under inert gas conditions. The reaction chamber was reduced to a base pressure of 5×10^{-4} Pa. High purity argon was pumped into the reaction chamber and a working gas pressure of 35 Pa was maintained during deposition. For double-cathode glow discharge deposition a voltage of −900 V was applied to the HEA target and a bias voltage of −300 V was applied to the substrate. A substrate temperature of 800 °C was employed. The distance between the substrate and the HEA target was held at 8.5 mm. The deposition time was 3 h.

2.2. Microstructural characterization

The microstructure of the HEA coating, in the as-deposited form, was characterized by a range of techniques. The crystal structure of the coating was investigated by X-ray diffractometry. A Bruker D8 Advance diffractometer, employing a Cu-Kα source was used. A current and voltage of 30 mA and 40 kV was applied to the X-ray source. The sample was cross-section and metallographically prepared and then subject to analysis by a Hitachi S-4800 scanning electron microscope (SEM). An EDX-4 energy dispersive spectroscopy (EDS) system was interfaced to this microscope. SEM analysis was also conducted on the surfaces of the coating and uncoated titanium substrate following cavitation-erosion testing. Transmission electron microscopy (TEM) was also undertaken on plan view specimens of the coating using a JEOL JEM-2010 instrument using a 200 kV accelerating voltage. TEM samples were prepared by sectioning, grinding, dimpling and then, as a final step, electrochemical polishing from the substrate side of the specimens. The composition and bonding state of surface layers formed on the coating following cavitation-erosion experiments were determined using X-ray photoelectron spectroscopy (XPS). An ESCALAB 250 system that employed an Al Kα X-ray source ($h\nu$ =1486.68 eV) was used. Spectra were calibrated with respect to adventitious carbon (the C1 s peak) at a binding energy of 284.6 eV. Peaks from survey scans and regional scans were identified with reference to a standard XPS database.

2.3. Mechanical properties

Nanoindentation testing was used to determine the hardness and elastic modulus of the as-deposited HEA coating. An Ultra-Micro test system, employing a pyramidal Berkovich diamond indenter was used. A maximum load of 20 mN was applied. Loading/unloading rate of 40 mN/min were used. Five measurements were performed to ensure reproducibility of the acquired data. Following testing values for hardness and modulus were calculated using the methods described by Oliver and Pharr [21]. Five indentations were conducted for each specimen to ensure reliability of the experimentally acquired data. The adhesion strength of the coating on the titanium substrate was measured by a commercial scratch tester (WS-2005), equipped with an acoustic emission (AE) detector. The scratch tests were performed with a 200 mm radius Rockwell C diamond indenter, which was drawn across the film surface using a linearly increased normal load from 0 N to 100 N. The loading rate was 20 N/min and a scratch speed was 1 mm/min. A critical load (Lc), defined as minimum load at which the coating failure occurs, was used to assess cohesion strength between the coating and the substrate. This parameter was assessed from both changes in the acoustic signal and SEM examination of scratch track.

2.4. Cavitation erosion tests

Ultrasonic cavitation tests were conducted in a magnetostrictive-driven apparatus (JY92-IIDN, NingBo Scientz Biotechnology Co., Ltd.)

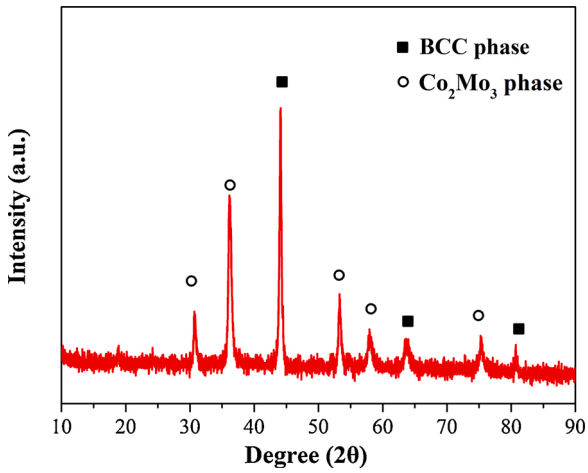

Fig. 1. Typical XRD pattern acquired from the CoCrFeNiTiMo HEA coating.

assisted by an electrochemical measurement system, consistent with ASTM standard G32−16. The frequency of horn resonance and a vibratory amplitude were maintained at 20 kHz and 60 μm, respectively. The specimen was mounted on a support table adjacent to the vibrating horn with the distance of 1 mm between the specimen and the horn. A naturally aerated 3.5 wt% NaCl solution was used as the test electrolyte. The solution temperature was maintained at 25 ± 1 °C controlled by flowing cooling water. The specimen was weighed at regular intervals of 2 h using an analytical balance (±0.01 mg), until the total test period of 12 h was reached.

2.5. Electrochemical measurement

All electrochemical testing were studied using an electrochemical workstation (CHI660C, Chenhua, Shanghai) using a three-electrode electrochemical cell configuration, which consisted of a working electrode with an area of exposure of ~1.0 cm^2, a platinum foil as counter electrode and a saturated calomel electrode (SCE) as reference electrode. The open circuit potential (OCP) of the sample in a 3.5 wt% NaCl solution was measured for 40 min to ensure that the E_{COP} value reaches steady-state. Potentiodynamic polarization was swept in the positive direction from an initial potential (300 mV lower than the corresponding E_{OCP} of the tested sample) to +1.2 V_{SCE} with a scanning rate of 20 mV/min. EIS measurements were undertaken using a perturbation amplitude of 10 mV and a range of frequencies that varied from 100 kHz to 0.01 Hz at each respective open circuit potential (OCP). The measured EIS data were evaluated by an appropriate electrical equivalent circuit (EEC) via ZSimpWin software.

3. Results and discussion

3.1. Microstructural characterization

Fig. 1 shows a typical X-ray diffraction (XRD) profile recorded from the CoCrFeNiTiMo HEA coating prepared onto a Ti-6Al-4 V substrate. After careful examination of the diffraction pattern, the recorded diffraction lines can be indexed as two phases with a body-centered cubic (BCC)-type solid solution phase and a tetragonal structured intermetallic Co_2Mo_3 phase, with the space group P42/mnm (136). By the linear extrapolation method, the lattice parameter of the BCC phase was calculated to be 2.898 Å, which is almost identical to that of α-(Fe, Cr) (JCPDF file No. 34-0396), 2.876 Å, and far less than that of the Co_2Mo_3 phase (a = 9.179 Å and c = 4.801 Å). The CoCrFeNiTiMo HEA system consists of various alloying elements with different crystal structures at ambient temperature, such as FCC-type Ni, BCC-type Fe, Cr, Mo and HCP-type Ti, Co. The crystal structure of this HEA system is highly dependent on the concentration of the different alloying elements and the interactions which occur among these elements. Previous studies revealed that some empirical parameters based on the solid solution theory, including atomic size difference(δ), mixing entropy (ΔS_{mix}), electronegativity difference (Δχ), mixing enthalpy (ΔH_{mix}) and valence electron concentration (VEC), can be used as powerful predictors of the presence of solid solution phases in HEAs. The calculated parameter values for the CoCrFeNiTiMo HEA are summarized in Table 1. In term of the three parameters, δ, ΔS_{mix} and ΔH_{mix}, the criteria for the solid solubility for a multi-component HEA should be in the appropriate range: $0 \le \delta \le 8.5$, $11 \le \Delta S_{mix} \le 19.5$ J/(K mol), $-22 \le \Delta H_{mix} \le 7$ kJ/mol and $\Omega > 1.1$ [22,23]. VEC values are known to be a parameter that can determine what type of solid solution phase is formed in HEAs: at VEC < 6.87 and VEC > 8, single BCC phase and single FCC phase will typically exist, and both phases will coexist in the region of 6.87 < VEC < 8.0 [24]. However, all these parameters here fail to effectively predict the CoCrFeNiTiMo HEA, which consists of a BCC solid solution together with an intermetallic compound. To understand the formation of possible intermetallic compounds in a HEA, Singh et al. [25] introduced a Λ-parameter ($\Lambda = \Delta S_{mix}/\delta^2$) calculated solely from geometrical information, and then used it to delineate the ranges for the formation of a single disordered solid solution phase (Λ>0.96), a mixture of solid solution phase and intermetallic compound (0.24 < Λ<0.96), and a single intermetallic compound (Λ<0.24). The Λ value of the CoCrFeNiTiMo HEA is calculated to about 0.44, locating in a zone for solid solution phase + intermetallic compounds, which is consistent with the XRD results. Furthermore, the electro-negativity reflects the ability of an atom to attract electrons towards it, and the more electronegative the alloying elements, the easier it is for an intermetallic compound to form in a HEA. Dong et al. [26] suggested that the electro-negativity difference (Δχ) could be regarded as a suitable parameter to predict the occurrence of ordered compounds. According to this criterion, the ordered compounds may occur at Δχ> 0.117, although more experimental data is needed to validate accuracy of this criterion. As listed in Table 1, the dual-phase structure of the CoCrFeNiTiMo HEA is satisfactorily predicted by the Δχ-parameter.

Table 1
The thermodynamic parameters of the CoCrFeNiTiMo alloy coating.

Alloy	δ (%)	ΔH_{mix} (kJ/mol)	ΔS_{mix} (J/mol K)	Δχ	VEC	Ω	Λ
CoCrFeNiTiMo	5.85	−13.33	14.90	0.196	7.17	2.30	0.44

Fig. 2 (a) presents a typical secondary electron image of cross-sectional morphology of the CoCrFeNiTiMo HEA coating deposited on a Ti-6Al-4 V substrate. The corresponding results of EDS line scan analysis and point analysis are shown in Fig. 2 (b), (c) and (d), respectively. It is clear that the as-prepared coating comprises a ~ 10 μm thick deposition layer and a diffusion layer ~ 2 μm in thickness, and both the sublayer and coating-substrate exhibit a compact form of bonding, free of any visible defects. From the higher resolution image of the deposited layer (inserted image in Fig. 2 (a)), two well-defined phases, namely a light grey strip-like region and a surrounding dark grey matrix, can be clearly identified. EDS analysis shows that the strip-like phase (marked as A) is rich in Mo and Ti, and a (Co + Cr + Fe + Ni)/(Mo + Ti) molar ratio of about 2/3 is broadly consistent with a stoichiometry of the form $(CoCrFeNi)_2(Mo,Ti)_3$. This indicates that the Mo atoms in the tetragonal Co_2Mo_3-type intermetallic compound can be replaced by Ti atoms, whilst the Co sites can be occupied by Cr, Fe and Ni atoms. As shown in Table 2, the mixing enthalpies of Ti and Mo with other alloy elements exhibit more negative values [27] and, simultaneously, Mo and Ti have a larger atomic radii than Co, Cr, Fe and Ni. Therefore, Mo and Ti prefer to enrich in the same phase and sit on equivalent lattice sites. The EDS spectrum from the darker phase, marked B, is seen to be richer in Co, Cr and Fe and leaner in Mo and Ti. Fig. 3(a) shows the plan-view

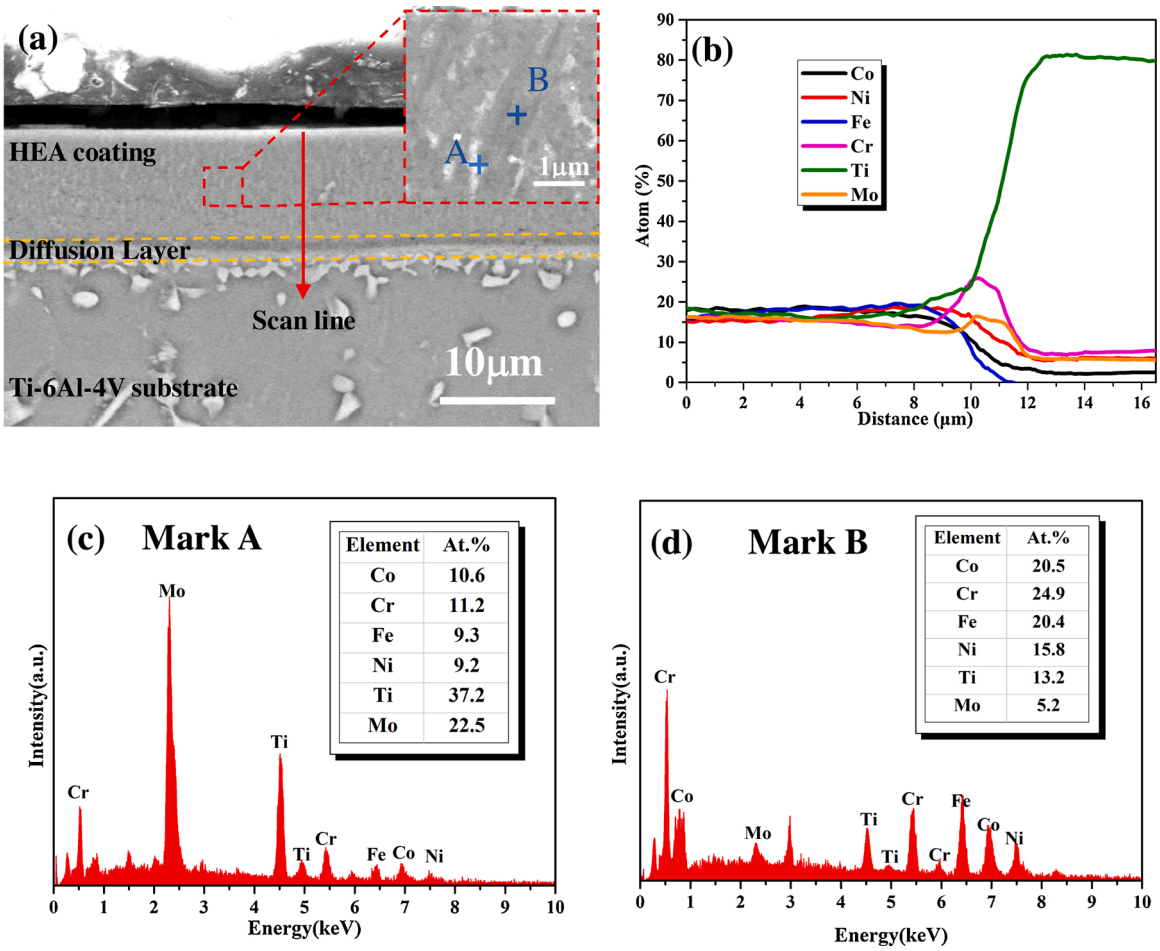

Fig. 2. (a) Typical SEM secondary electron image of cross-sectional morphology of the CoCrFeNiTiMo HEA coating deposited on a Ti-6Al-4 V substrate, together with (b) the EDS line scan analysis of the HEA coating and EDS point analysis of regions marked (c) A and (d) B in Fig. 2(a).

Table 2
The values of $\Delta H^{mix}_{(AB)}$ (kJ/mol) calculated by Miedema's model for atomic pairs between elements with atomic numbers [27].

$\Delta H^{mix}_{(AB)}$ (kJ/mol)	Co	Cr	Fe	Ni	Ti	Mo
Co	–	–	–	–	–	–
Cr	−4	–	–	–	–	–
Fe	−1	−1	–	–	–	–
Ni	0	−7	−2	–	–	–
Ti	−28	−7	−17	−35	–	–
Mo	−5	−0	−2	−7	−4	–

bright-field TEM images of the as-deposited CoCrFeNiTiMo HEA coating. It is observed that two phases are present in the coating: a grey strip-like phase and the surrounding matrix phase. The higher magnification image (Fig. 3(b)) reveals that the strip-like phase consists of spherical crystallites with sizes in the range of 8−20 nm. A HRTEM lattice image (Fig. 3(c)) and the corresponding fast Fourier transformation (FFT) pattern (inset of Fig. 3(c)) indicate that two measured inter-fringe distances in marked region are measured to be as 2.41 Å and 2.91 Å with the corresponding dihedral angle of 90°, which are consistent with the lattice spacings of (002) and (310) planes for the tetragonal structured Co_2Mo_3 phase. For the matrix phase shown in Fig. 3(d), (200) lattice fringes d =1.45 Å and (110) lattice fringes with d =2.05 Å with the corresponding dihedral angle of 45° are clearly observed, and the diffraction spots obtained through fast Fourier transform (FFT) was consistent with a BCC structure oriented parallel to the [001] zone axis.

3.2. Mechanical characterization

3.2.1. Nano-indentation tests

To assess the effect of the presence of Co_2Mo_3 phase on the hardness of the HEA coating, nano-indentation tests were conducted on the high-entropy matrix phase, the Co_2Mo_3 phase and the overall coating, as shown in Fig. 4. For comparison, uncoated Ti-6Al-4 V alloy was also evaluated under a maximum load of 100 mN. It can be seen from the recorded load–displacement curves under a maximum load of 20 mN shown in Fig. 4(a) that a higher applied indentation force is required for the Co_2Mo_3 phase to impose the same depth displacement as compared to the high-entropy matrix phase. Further, the amount of elastic recovery on unloading plot is also reduced from 49.6 % for the high-entropy matrix phase to 42.5 % for the Co_2Mo_3 phase, indicating that the high-entropy matrix phase is of lower hardness. Similarly, from the recorded load–displacement curves of the overall coating and Ti-6Al-4 V substrate (Fig. 4(b)), under a peak load of 100 mN, the maximum penetration depth of the indenter for the coating is clearly shallower than that for the Ti-6Al-4 V substrate, indicative of a greater resistance to local plastic deformation for the coating. Hardness (H) and elastic modulus (E) values for the tested samples, determined by the recorded load–displacement curves based on the procedure proposed by Oliver-Pharr [21], are shown in the inserted tables in both Fig. 4(a) and (b). The results show that Ti-6Al-4 V substrate has the lowest hardness among the tested samples, and the Co_2Mo_3 phase is ~1.5 times harder than the high-entropy matrix phase. The hardness of the high-entropy matrix

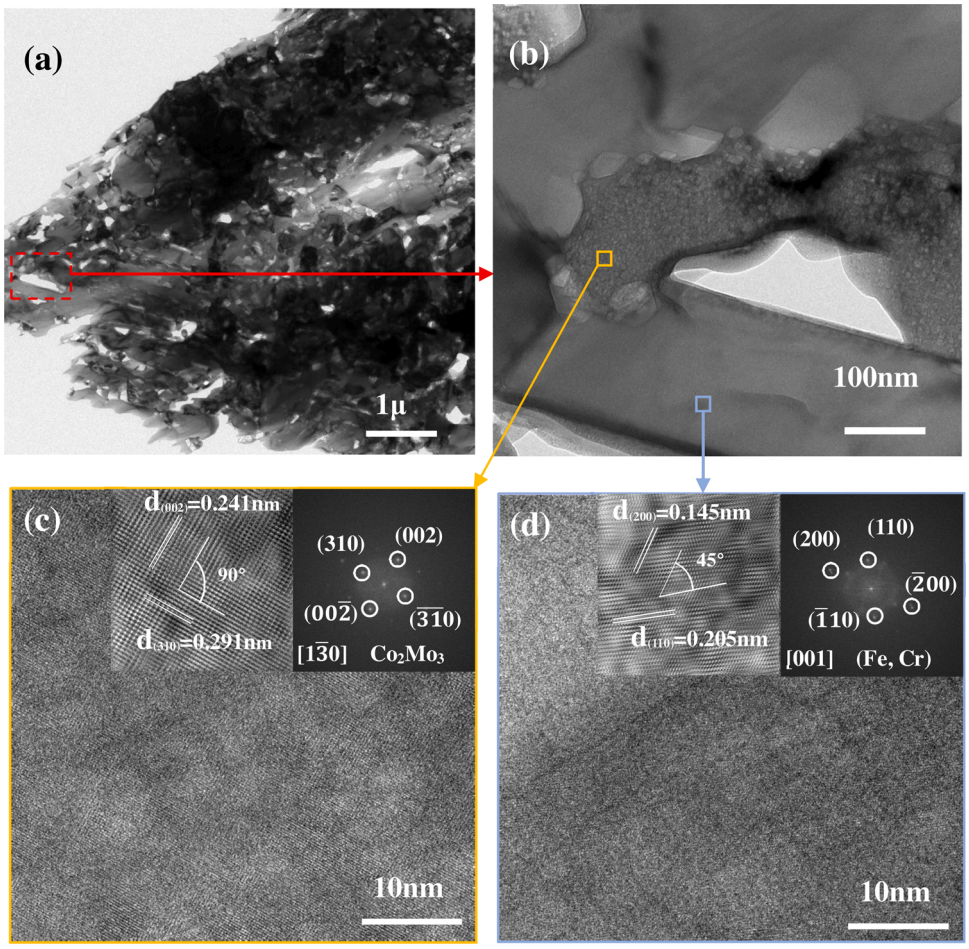

Fig. 3. (a) Plan-view bright-field TEM image and (b) the higher magnification image of the as-deposited CoCrFeNiTiMo HEA coating. HRTEM lattice images and the corresponding fast Fourier transformation (FFT) patterns (inset) for (c) the strip-like phase and (d) the matrix phase.

phase is comparable to, or larger than, that reported for some high-entropy alloys with similar components, such as $CoCrFeNiAl_xTi_y$ HEA (283~ 859 H_V) [28], AlCoFeNiMoTi HEA (681 H_V) [10] and AlFeNiCuCr HEA (762 H_V) [29]. Further, Guo et al. [11] investigated the mechanical properties of CoCrFeNiMn HEA matrix composites with the addition of Cr_3C_2. They found that when the volume fraction of Cr_3C_2 increased from 0 to 10 %, 20 % and 40 %, the Vickers hardness of the CoCrFeNiMn HEA matrix composites increased correspondingly from 181.2 H_V to 323.2, 417.0 and 681.6 H_V. Cheng et al. [30] also studied the effect of in situ synthesized TiC–TiB_2 on the hardness of CoCrCuFeNi HEA composite coatings. Their results suggested that the hardness increased from 4.19 GPa for the CoCrCuFeNi(Ti, $B_4C)_{0.1}$ coating to 9.14 GPa for the CoCrCuFeNi(Ti, $B_4C)_{0.5}$ coating. In our case, the hardness value of the overall coating lies between the values for the Co_2Mo_3 phase and the high-entropy matrix phase, and increased by ~30 % as compared with the high-entropy matrix phase, which indicates that the presence of nanoscale Co_2Mo_3 phase acts as strengthening phase to improve the hardness of coating. Significant efforts have been made to correlate the cavitation erosion rate and the mechanical properties of a material, and the results have shown that the cavitation erosion resistance of a material is not only related to its hardness [31], but also associated with its ratio of hardness/elastic (H/E) and elastoplasticity [32,33]. A material with a larger H/E value denotes that it will undergo larger elastic strain before failure induced by subsequent plastic deformation and fracture, and thus it possesses a higher capability to resist contact pressures when subjected to cavitation damage. Furthermore, the elastoplasticity of a material, evaluated by its energy recovery ratio (η), reflects its ability to absorb the impact energy released by the implosion of bubbles under cavitation erosion conditions [33]. The η value is calculated as the ratio of the elastic deformation energy (that is, the area under the unloading curve) relative to the total deformation energy (that is, the area under the loading curve). As shown in the inserted tables in Fig. 4(b), the H/E ratio and η value of the HEA coating are greater than those for Ti-6Al-4 V and, comparatively the CoCrCuFeNi(Ti, $B_4C)_{0.5}$ HEA composite coating studied by Cheng et al. [30], which suggests that the HEA coating developed here may be expected to exhibit a higher impact load absorbing capacity.

3.2.2. *Scratch tests and contact damage resistance*

For the hard coating/soft substrate systems, the coating/substrate adhesion strength is another parameter that can determine the in-service performance of the coated metallic components used under cavitation erosion ambient conditions. Under such conditions, the interfacial area between coating and substrate, commonly considered as a weak location, is liable to detach under high energy impacting environment generated by the collapse of bubbles [34]. Hence, excellent adhesion to the substrate is an extremely important property with regard to the high reliability of a coated substrate applied in a hostile environment. The depth-sensing scratch tester was used to test the HEA coating/substrate adhesion strength and a critical normal load (L_c) for the HEA coating failure was determined by acoustic emission recording with the help of SEM observation of the scratch track. From the entire residual scratch track morphology (inset of Fig. 5), the width of the scratch track and the penetration depth of the diamond stylus increase with progressive increases in normal load. At an applied normal load less than the Lc value, the morphology of the scratch track appears smooth with no evidence of

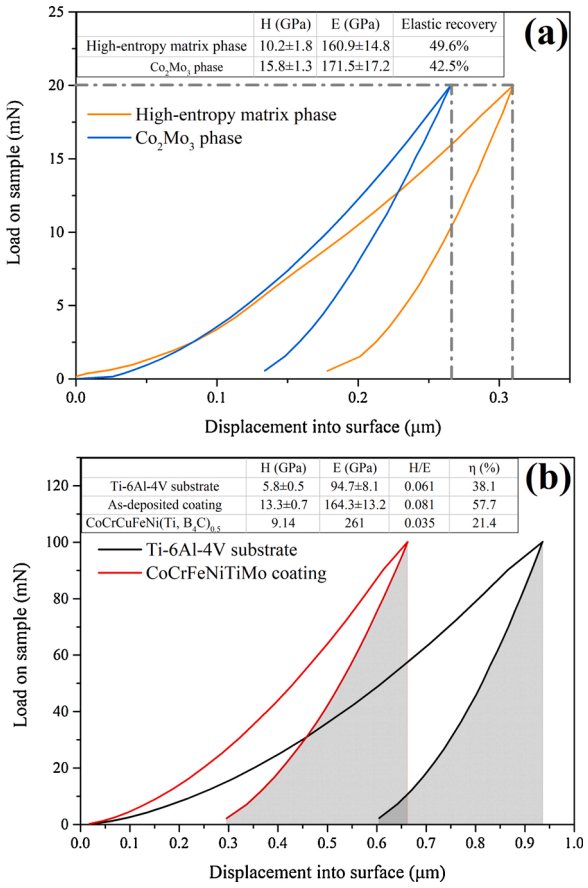

Fig. 4. (a) Load–displacement curves recorded from the high-entropy matrix phase, Co_2Mo_3 phase under a maximum load of 20 mN. (b) The load–displacement curves recorded from the overall CoCrFeNiTiMo HEA coating and the uncoated Ti-6Al-4 V alloy under a maximum load of 100 mN.

severe damage. However, as the normal load increases to 70 N, the first occurrence of cracks is accompanied by an abrupt increase in the acoustic emission signal. These parallel cracks are initiated by tensile stresses occurring at the rear of the diamond stylus. Further chipping occurs at the edge of the scratch track with further increases in the applied normal load. No severe wedging spallation was detected up to a maximum normal load of 100 N, suggesting that the HEA coating has a high load bearing capacity and provides sufficient resistance to abrasion damage for applications involving heavy loading conditions. Additionally, to investigate the contact damage resistance of the HEA coating, Vickers indentation tests were undertaken on the coating with different applied loads ranging from 0.49 N to 9.8 N, as shown in Fig. 5. This clearly shows that when the applied normal force is below 4.9 N, no cracks emanate from the surrounding impression of the Vickers indentation. However, when the applied normal force is equal to, or greater than, 4.9 N, ring-shaped cracks are visible around the indentation impressions. Krella et al. [35] found that the critical load at which no cracks occurred during the Vickers indentation test was 0.39 N for cavitation resistant Cr-N coatings prepared by a cathodic arc evaporation method. Hence, compared with those coatings, the HEA coating exhibits a much greater threshold value for crack formation.

3.3. Electrochemical corrosion during cavitation erosion tests

3.3.1. Current-time responses and open circuit potential (OCP)

The influences of cavitation intensity on the current densities and open circuit potentials of the tested samples were carried out in a 3.5 wt %NaCl solution under experimental conditions, where the applied

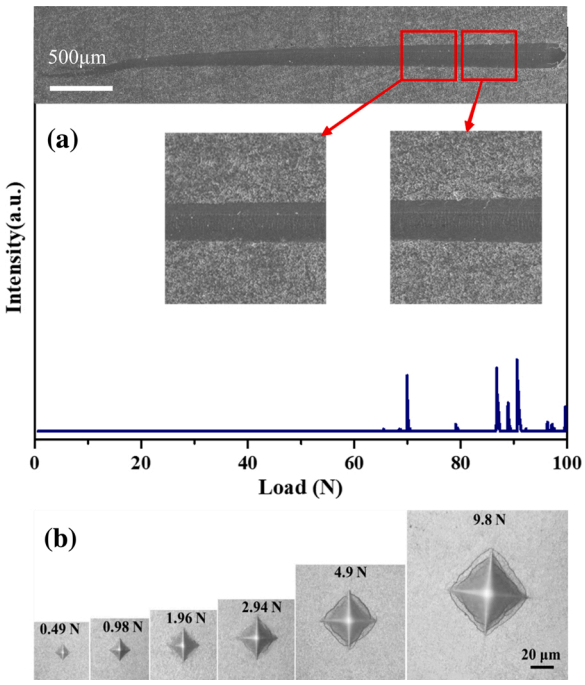

Fig. 5. (a) Acoustic emission signal peaks versus normal load curve for the CoCrFeNiTiMo HEA coating and SEM image of the scratch track and region around a critical load were shown inset. (b) SEM image of the Vickers indentation on the coating with applied different loads ranging from 0.49 N to 9.8 N.

output power as a function of cavitation time is shown in Fig. 6(a). Fig. 6 (b) shows the current–time transients recorded for the HEA coated and uncoated Ti-6Al-4 V substrate potentiostatically anodized at a potential of 0.3 V under different output powers in a 3.5 wt% NaCl solution. For bare Ti-6Al-4 V, the current decreases with exposure time in a static 3.5 wt% NaCl solution, which is related to passive film grown on the sample surface, and under ultrasonic cavitation conditions, with increasing output powers, the current density rises step by step and its fluctuation amplitude increases. However, the current-time plot for the HEA coating is almost smooth and the cavitation effect has little influence on the current density of the coating. The current densities of the HEA coating under both a static solution and cavitation conditions are very small, of the order of 10^{-7}A/cm^2, which is one order of magnitude lower than that for bare Ti-6Al-4 V. This demonstrates a significantly lower metal dissolution rate for the HEA coating compared to the uncoated sample. During cavitation in a corrosive medium, an increase in current density arises from additional corrosion due to the erosion attack that makes the surface exposed to the corrosive medium more anodic. Hence, compared to the uncoated alloy, the HEA coating has less sensitivity to cavitation erosion in aqueous corrosive environments.

Fig. 6(c) presents the open circuit potential (E_{OCP}) values versus cavitation time plots obtained from the HEA coated and uncoated Ti-6Al-4 V alloy under different output powers in a 3.5 wt% NaCl solution. As shown in Fig. 6(c), it is clear that the E_{OCP} versus cavitation time plots for both specimens are similar in shape, suggesting that both of them undergo a similar corrosion process. At the onset of the experiment, namely in stagnant conditions, the two samples exhibit a sharp increase of E_{OCP} to more positive values and then rate of increase of E_{OCP} slows down until the cavitation process commences. Once cavitation begins, E_{OCP} shows a sudden decrease and subsequently maintains a relatively stable value. A drop in E_{OCP} is largely because of mechanical rupture induced by impact from the collapsing bubbles that can act to remove the passive films formed on both specimens. Whether under a static solution or cavitation conditions, the E_{OCP} value recorded on the HEA coating was always higher than that recorded from the uncoated Ti-6Al-4 V alloy. This suggests that a more mechanically robust and

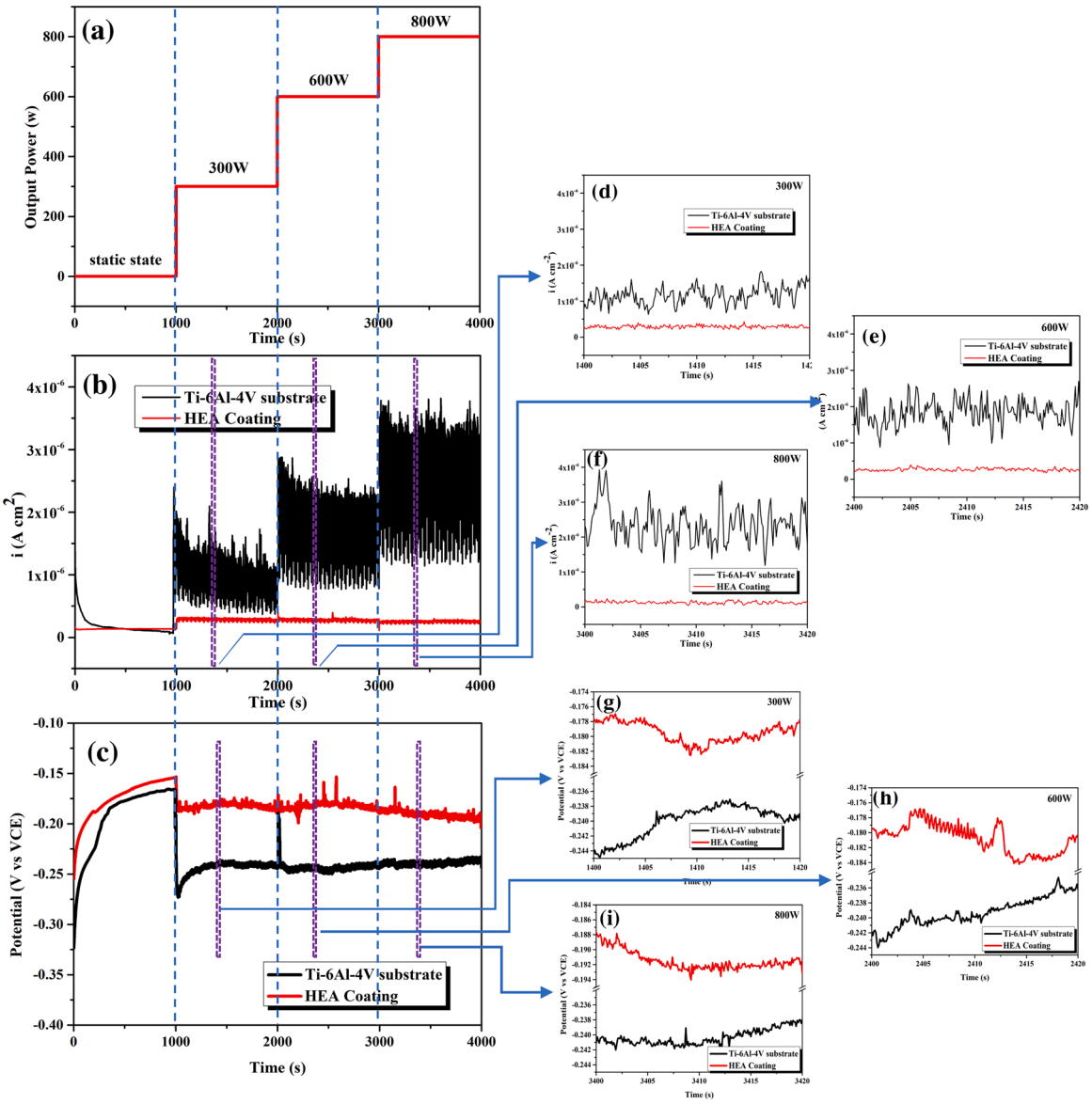

Fig. 6. (a) The applied output power as a function of cavitation time curve. (b) The current–time transients recorded for the HEA coated and uncoated Ti-6Al-4 V alloy potentiostatically anodized at a potential of 0.3 V under different output powers in 3.5 wt% NaCl solution. (c) The E_{OCP} vs. cavitation time plots obtained from the HEA coated and uncoated Ti-6Al-4 V alloy under different output powers in 3.5 wt% NaCl solution. The higher magnification plots of the (d-f) current-time curves and the (g-i) E_{OCP}-time curves for a duration of 20 s at the cavitation output power of (d, g) 300 W, (e, h) 600 W and (f, i) 800 W.

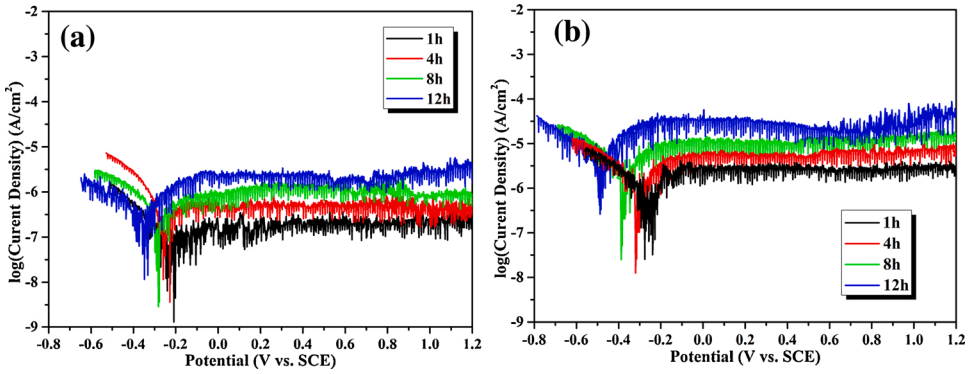

Fig. 7. The potentiodynamic polarization plots of (a) the HEA coated and (b) uncoated Ti-6Al-4 V alloy at a given output power of 800 W after different cavitation times in 3.5 wt% NaCl solution.

Table 3
The electrochemical parameters obtained from the polarization curves of the HEA coated and uncoated Ti-6Al-4 V alloy.

	Cavitation Time	$E_{corr}(V_{SCE})$	$i_{corr}(Acm^{-2})$
TC4	1h	−0.256	1.44×10^{-6}
	4 h	−0.321	2.78×10^{-6}
	8 h	−0.388	6.92×10^{-6}
	12 h	−0.487	1.02×10^{-5}
Coating	1h	−0.209	1.31×10^{-7}
	4 h	−0.228	2.92×10^{-7}
	8 h	−0.282	6.52×10^{-7}
	12 h	−0.348	9.82×10^{-7}

protective passive film is grown on the HEA coating, thereby mitigating damage caused by cavitation impingement.

3.3.2. *Potentiodynamic polarization tests*

Fig. 7 displays the potentiodynamic polarization plots of the HEA coated and uncoated Ti-6Al-4 V alloy at a given output power of 800 W after different cavitation times in a 3.5 wt% NaCl solution. It is clear from Fig. 7 that, with increasing cavitation times, the anodic branches of the polarization plots of both the HEA coated and uncoated Ti-6Al-4 V move to a more negative direction and simultaneously shift upwards to regions with higher current density, indicating that the presence of ultrasonic cavitation erosion stimulates anodic reaction for the tested samples. Moreover, all the measured polarization plots show significant variation in amplitude, characterized by some spikes in current for both the cathodic and anodic branches. For the cathodic branches, two cathodic reactions exist, namely, for oxygen reduction ($O_2+2H_2O+4e \leftrightarrow 4OH^-$) and hydrogen evolution ($2H_2O + 2e \leftrightarrow H_2 + 2OH^-$) [36,37]. The two cathodic reactions have divergent influence on the cathodic current density of a material under cavitation-erosion condition. In this case, the cathodic current density can be increased by the accelerated oxygen reduction reaction due to the enhanced mass transfer of dissolved oxygen and adsorption of the reductants on the sample surface. On the other hand, the hydrogen gas generated from the hydrogen evolution reaction cushion the impact of the cavitation bubble collapse and this reduces the total current density [38]. For uncoated Ti-6Al-4 V, the cathodic current density increases with increasing cavitation time, suggesting that the cathodic reaction is regulated by the oxygen reduction. Instead, the cathodic current density of the HEA coating is not appreciably affected by an increase in cavitation time, except for a slight increase after 4 h of cavitation time. The reasons for this phenomenon are two-fold: (1) the required electrons of the cathodic reaction are provided by the anodic oxidation reaction, and low anodic reaction rate of the coating inhibits the cathodic reaction process; (2) with the extension of cavitation time, the cathodic branches shift toward more negative potential, which enhances the hydrogen evolution and further increases the cushioning effect of hydrogen gas [39]. A similar phenomenon has also been observed by other researchers [40,41]. In the case of the anodic branches, the adsorbed anions, including O^{2-} or OH^- on the passive films, accelerate the anodic reaction and shift the anodic branches to a higher current density region. All the measured current density values of the two tested samples at different cavitation times are less than 100 μA/cm^2, which is generally regarded as the threshold value for the onset of pitting corrosion. Thus, the passive oxide films are important in protecting the samples from undergoing active corrosion under cavitation conditions. As cavitation time increases, the repeated cavitation impingement can disrupt the surface passive films on the tested samples, making them porous and loose, eventually delaminating from the sample surface. Therefore, application of cavitation conditions renders the samples surface more electrochemically active and stimulates an increase in anodic current density. The corresponding electrochemical parameters acquired from the polarization curves shown Fig. 7, including corrosion potential (E_{corr}) and corrosion current density (i_{corr}), are presented in Table 3. It is shown with increasing cavitation time, the E_{corr} value tends to decrease and the i_{corr} value increases. At a given cavitation time, the HEA coating exhibits a lower i_{corr} and more positive E_{corr} than uncoated Ti-6Al-4 V. This is attributed to the passive film on the HEA coating that is both continuous and more protective compared to uncoated Ti-6Al-4 V, which thus gives the coating higher resistance against the combined action of electrochemical reaction and mechanical impact under cavitation conditions.

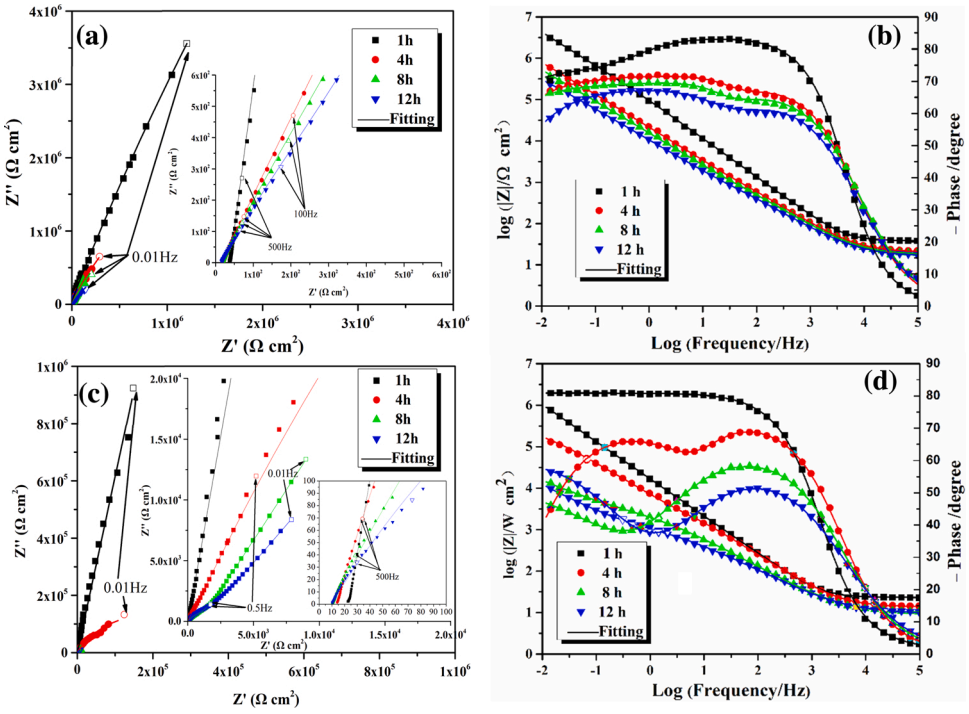

Fig. 8. The EIS data taken from (a and b) the HEA coating and (c and d) the reference Ti-6Al-4 V, after different cavitation periods in 3.5 wt% NaCl at output power of 800 W, presented in the form of (a and c) Nyquist, and (b and d) Bode plots.

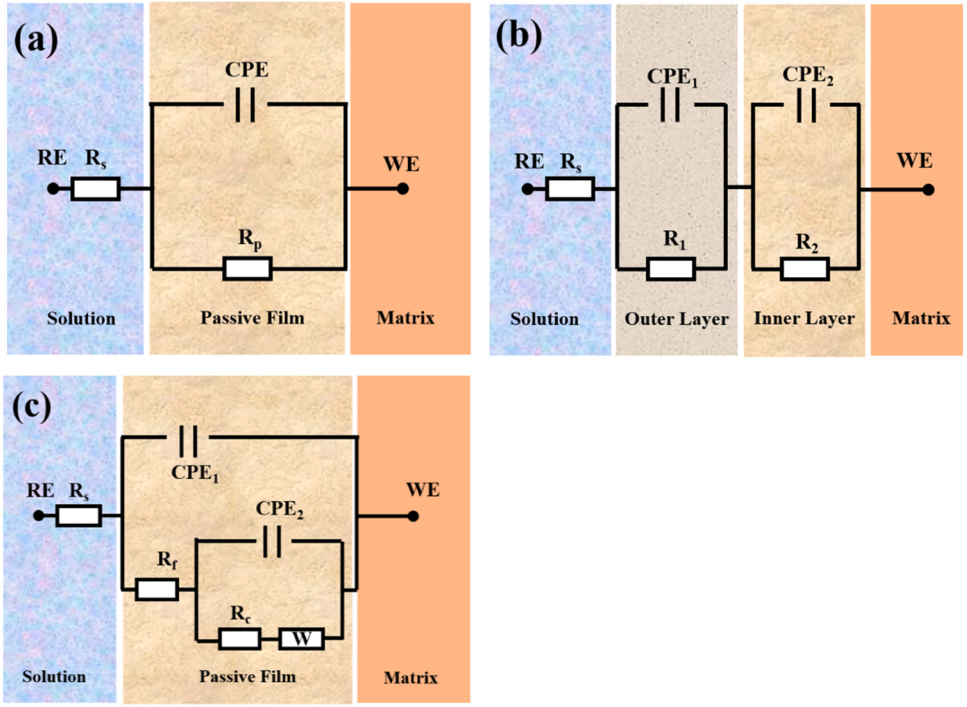

Fig. 9. The proposed equivalent electron circuit (EEC) used to model the measured impedance data. (a) $R_s(R_pCPE)$ for the impedance spectra for both coated and uncoated Ti-6Al-4 V after 1 h of cavitation. (b) $R_s(R_1CPE_1)(R_2CPE_2)$ for the uncoated Ti-6Al-4 V after 4 h of cavitation and the HEA coating after 4 h, 8 h and 12 h of cavitation. (c) $R_s(CPE_1(R_f(CPE_2(R_cW))))$ for the uncoated Ti-6Al-4 V after 8 h and 12 h.

3.3.3. *Electrochemical impedance spectroscopy (EIS) tests*

The EIS data taken from the HEA coating and the reference Ti-6Al-4 V substrate, after different cavitation periods in a 3.5 wt% NaCl at an output power of 800 W, are given in the form of Nyquist, and Bode plots shown in Fig. 8. As shown in Fig. 8 (a) and (c), all the Nyquist plots show typical semicircles over the entire frequency range and the diameters of the capacitive arcs for both samples decrease with increasing the cavitation periods. Accordingly, from the Bode phase angle diagrams (shown in Fig. 8 (b) and (d)), the maxima of the phase angle plots for both samples also decrease with increasing the cavitation periods. Generally speaking, the size of the semicircle diameter reflects charge-transfer reaction and quality of the passive films grown on the sample surface. That is, the larger semicircle diameter, the stronger corrosion resistance [42]. Likewise, the maximum value of phase angle in the medium frequency region is a reflection of the capacitive behavior of the impedance at this frequency region; that is, the larger phase angle maximum, the better insulating properties. Therefore, the cavitation process reduces the protectiveness of the passive films that form on the samples during testing.

To obtain the quantitative analysis of electrochemical reactions occurred at the sample/electrolyte interface, the measured impedance data were modeled with the proposed equivalent electron circuit (EEC) using ZsimpWin software. The impedance spectra for both coated and uncoated Ti-6Al-4 V after 1 h of cavitation exhibits a single time constant in the frequency range 10^{-2}–10^{5} Hz and can be modeled using an equivalent circuit model (shown in Fig. 9(a)). This consists of a constant phase element (CPE) in parallel with a resistance R_p. Inspection of the recorded Bode phase (phase angle vs. frequency) plots for uncoated Ti-6Al-4 V after 4 h of cavitation and the HEA coating after cavitation periods of 4 h, 8 h and 12 h, phase angle maxima in the low and middle

Table 4
The values of equivalent circuit parameter determined by fitting analysis of impedance spectra obtained from the HEA coating and the reference Ti-6Al-4 V after different cavitation periods.

TC4		$R_s(R_pCPE)$							
		R_s (Ωcm^2)	CPE ($\Omega^{-1}cm^{-2}s^{-n}$)	n	R_p (Ωcm^2)				
	1h	23.12	1.14×10^{-5}	0.80	2.59×10^{6}				
		$R_s(R_1CPE_1)(R_2CPE_2)$							
		R_s (Ωcm^2)	CPE_1 (Ω^{-1} cm^{-2} s^{-n})	n_1	R_1 (Ω cm^2)	CPE_2 (Ω^{-1} $cm^{-2}s^{-n}$)	n_2	R_2 (Ω cm^2)	
	4h	14.08	1.71×10^{-5}	0.67	2.56×10^{3}	1.84×10^{-5}	0.78	3.16×10^{5}	
		$R_s(CPE_1(R_f(CPE_2(R_cW))))$							
		R_s (Ωcm^2)	CPE_1 (Ω^{-1} cm^{-2} s^{-n})	n_1	R_f (Ω cm^2)	CPE_2 (Ω^{-1} $cm^{-2}s^{-n}$)	n_2	R_c (Ω cm^2)	W (Ω^{-1} $cm^{-2}\sqrt{s}$)
	8h	12.13	4.32×10^{-5}	0.61	2.07×10^{3}	3.37×10^{-5}	0.70	2.16×10^{4}	5.01×10^{-3}
	12h	11.58	1.12×10^{-4}	0.59	1.84×10^{3}	4.64×10^{-5}	0.62	1.51×10^{4}	8.94×10^{-3}
		$R_s(R_pCPE)$							
		R_s (Ωcm^2)	CPE ($\Omega^{-1}cm^{-2}s^{-n}$)	n	R_p (Ωcm^2)				
	1h	38.1	1.85×10^{-6}	0.93	1.29×10^{7}				
Coating		$R_s(R_1CPE_1)(R_2CPE_2)$							
		R_s (Ωcm^2)	CPE_1 (Ω^{-1} cm^{-2} s^{-n})	n_1	R_1 (Ω cm^2)	CPE_2 (Ω^{-1} $cm^{-2}s^{-n}$)	n_2	R_2 (Ω cm^2)	
	4h	20.05	1.05×10^{-5}	0.79	1.07×10^{5}	3.74×10^{-6}	0.89	7.76×10^{6}	
	8h	17.38	1.50×10^{-5}	0.76	9.85×10^{4}	2.79×10^{-5}	0.87	7.22×10^{6}	
	12h	16.18	2.09×10^{-5}	0.74	4.54×10^{4}	6.31×10^{-5}	0.86	1.45×10^{6}	

Table 5
The effective capacitance, C_{eff}, and thickness, d_{eff}, of the passive films for the HEA coating and the uncoated Ti–6Al–4 V substrate after different cavitation times in 3.5 wt% NaCl at an output power of 800 W.

		1h	4 h	8 h	12 h
C_{eff} (μF cm^{-2})	Uncoated Ti–6Al–4V	26.6	39.4	43.8	174.8
	HEA coating	2.4	10.8	17	20.5
d_{eff} (nm)	Uncoated Ti–6Al–4V	2.26	1.52	1.35	0.34
	HEA coating	9.58	2.13	1.37	1.12

frequency ranges are recognizable, reflecting two time constants in the entire frequency range. Based on the above analysis, these experimental impedance spectra were modeled using an equivalent circuit composed of the two RC circuits presented in Fig. 9(b). This model assumes the formation of bilayer structured oxide layer that is composed of a dense inner barrier layer and a porous outer layer. In the equivalent circuit $R_s(R_1CPE_1)(R_2CPE_2)$, R_s is the solution resistance, R_1 and CPE_1 are the resistance and the non-ideal capacitance of the porous outer layer, respectively, R_2 and CPE_2 are the resistance and the non-ideal capacitance of the inner barrier layer, respectively. For bare Ti-6Al-4 V after 8 h and 12 h of cavitation, the Nyquist impedance plots consist of a single semicircle over the high frequency region and diffusive tail in the low frequency region, suggesting that typical Warburg character appears after cavitation periods of 8 h and 12 h. The presence of a Warburg tail signifies either the diffusion of the aggressive species through the defects in the passive film on Ti-6Al-4 V or dissolution reactions of Ti-6Al-4 V. For the two impedance spectra plots, the first time-constant is associated with corrosion process of the passive films, and the second one is related to the corrosion process at the passive film/Ti-6Al-4 V interface. Hence, the equivalent circuit model, shown in Fig. 9(c), was employed to describe the measured EIS spectra on bare Ti-6Al-4 V after 8 h of cavitation. In this equivalent circuit, R_s is the electrolyte resistance, R_f is the resistance of passive film, CPE1 represents the non-ideal capacitance for the capacitance of passive film, R_c is the charge transfer resistance, CPE_2 is the non-ideal capacitance for double-charge layer, and W is the Warburg impedance. Table 4 gives the values of the equivalent circuit parameter determined by fitting the analysis of the impedance spectra obtained from the HEA coating and the reference Ti-6Al-4 V after different cavitation periods. It is clear that the resistance values of both the HEA coating and bare Ti-6Al-4 V were lowered with increasing the cavitation periods, indicating that the passive films that form on these samples became less dense and provide lower protective performance. Passive films that exhibit a porous structure provide short-circuiting paths for the penetration of corrosive species from the electrolyte and this leads to a smaller semicircle diameter for the Nyquist plots with increasing cavitation periods. For a given cavitation period, the resistance value for the HEA coating is about an order of magnitude higher than that for bare Ti-6Al-4 V, indicating that the HEA coating has higher resistance to prevent damage from corrosion under cavitation conditions.

Potucek et al. have argued that the resistance (R) values obtained from EIS data are highly dependent on the solution in which the measurements are made, while the capacitance (C) values are independent of the solution conditions [43]. Therefore, the C values are shown to be a much more reliable means of determining the passive film thickness. According to the work of Orazem et al. and Hsu et al., the effective capacitance (C_{eff}) can be extracted from the CPE parameters using the following equation [44,45]:

$$C_{eff} = Q^{1/\alpha} R_f^{(1-\alpha)/\alpha} \quad (1)$$

where R_f is the film resistance, Q and α are CPE parameters. The thickness of the passive film d_{eff} can be calculated as follows [46]:

$$C_{eff} = \frac{\varepsilon_r \varepsilon_0}{d_{eff}} \quad (2)$$

where ε_0 ($8.8542 \times 10 - 14$ F/cm) is the permittivity of vacuum and ε_r is the dielectric constant of the passive film. The ε_r value for the passive film HEA coating is 23, that is determined from the mixture rule [47] and the passive film composition derived from XPS measurements (presented in section 3.3.5). The value of ε_r is 60 for Ti-6Al-4 V is the value reported in Ref [48]. The calculated results are listed in Table 5. It is clear that the thickness of the passive films for both the uncoated Ti-6Al-4 V and the HEA coating decrease with increasing cavitation time. A thicker passive film was formed on the HEA coating than that on the uncoated Ti-6Al-4 V for any given cavitation time.

3.3.4. Potential of zero charge (PZC) measurements

Considering that the ultrasonic cavitation experiments were tested in a chloride containing medium, it is necessary to evaluate the adsorption behavior of negatively charged chloride ions on the tested samples, since the adsorbed chloride ions can make the passive films unstable and lead to their localized breakdown. According to the Gouy–Chapman theory [49], the potential of zero charge (PZC) is an important parameter to assess the adsorption capability of a material to both charged and neutral species. PZC corresponds to a potential at which the sample surface has no excess charge, and can be determined by double-layer capacity measurements. Fig. 10 presents the double-charge layer capacitance as a function of applied potential for the HEA coating and the Ti-6Al-4 V reference alloy after 12 h of cavitation in a 3.5 wt% NaCl at output power of 800 W. As shown in Fig.10, both the double-layer capacity versus potential plots have a pronounced minimum, corresponding to the PZC values of the tested samples. Apparently, the PZC values for the two samples are more positive than their respective E_{corr} value denoting that the surfaces of both samples are negatively charged at their respective E_{corr} and would therefore repel chloride ions from their surfaces. The potential differences between E_{corr} and PZC (ΔE =

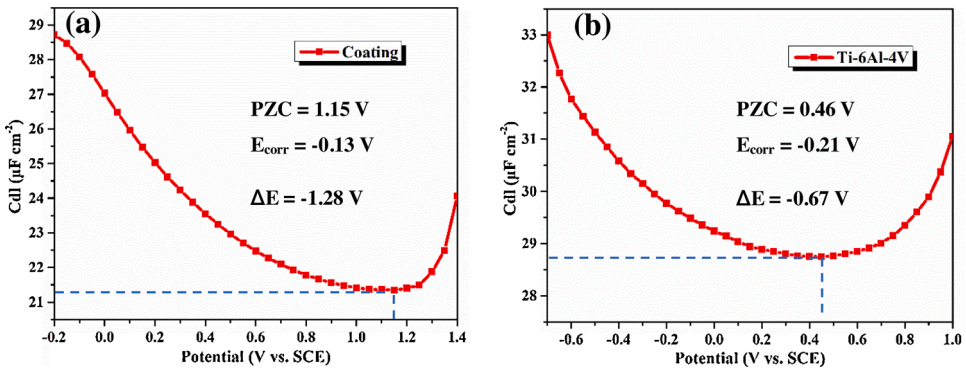

Fig. 10. The double-charge layer capacitance as a function of applied potential for the HEA coating and the reference Ti-6Al-4 V after 12 h of cavitation in 3.5 wt% NaCl at output power of 800 W.

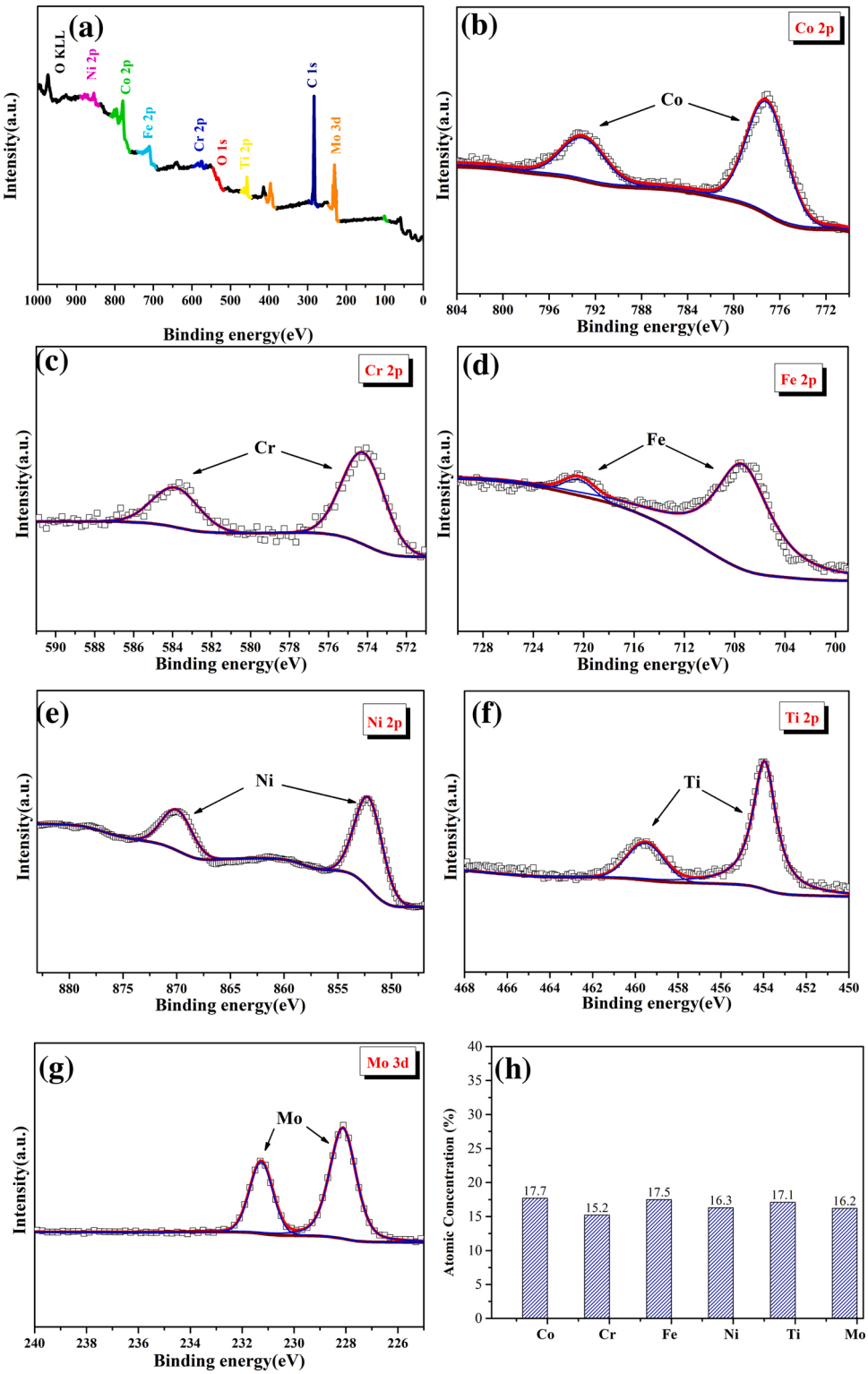

Fig. 11. XPS analysis was performed on the as-prepared HEA coating. (a) The XPS survey spectrum, (b-g) the high-resolution XPS spectra assigned to Co 2p, Cr2p, Fe 2p, Ni 2p, Ti 2p and Mo 3d, respectively. (h) The content of the metal elements presents in the as-prepared HEA coating.

E_{corr} PZC) are -1.28 V and -0.67 V for the HEA coating and the titanium reference alloy, respectively, suggesting that the HEA coating shows a higher ability to impede the absorption of chloride ions.

3.3.5. *XPS analysis*

To investigate the influence of cavitation on the chemical composition as well as the chemical state of the elements on the surface of the HEA coating, XPS analysis was performed on the as-prepared coating (Fig. 11) and the eroded coating (Fig. 12) after 12 h of cavitation in a 3.5 wt% NaCl at an output power of 800 W. In the XPS wide-scan survey spectrum (Fig. 11 (a)), Co 2p, Cr 2p, Fe 2p, Ni 2p, Ti 2p, Mo 3d and C 1s peaks were detected on the surface of the as-deposited coating. According to the core level spectra for Co 2p, Cr 2p, Fe 2p, Ni 2p, Ti 2p and Mo 3d recorded from the as-prepared coating (Fig. 11 (b–g)), the

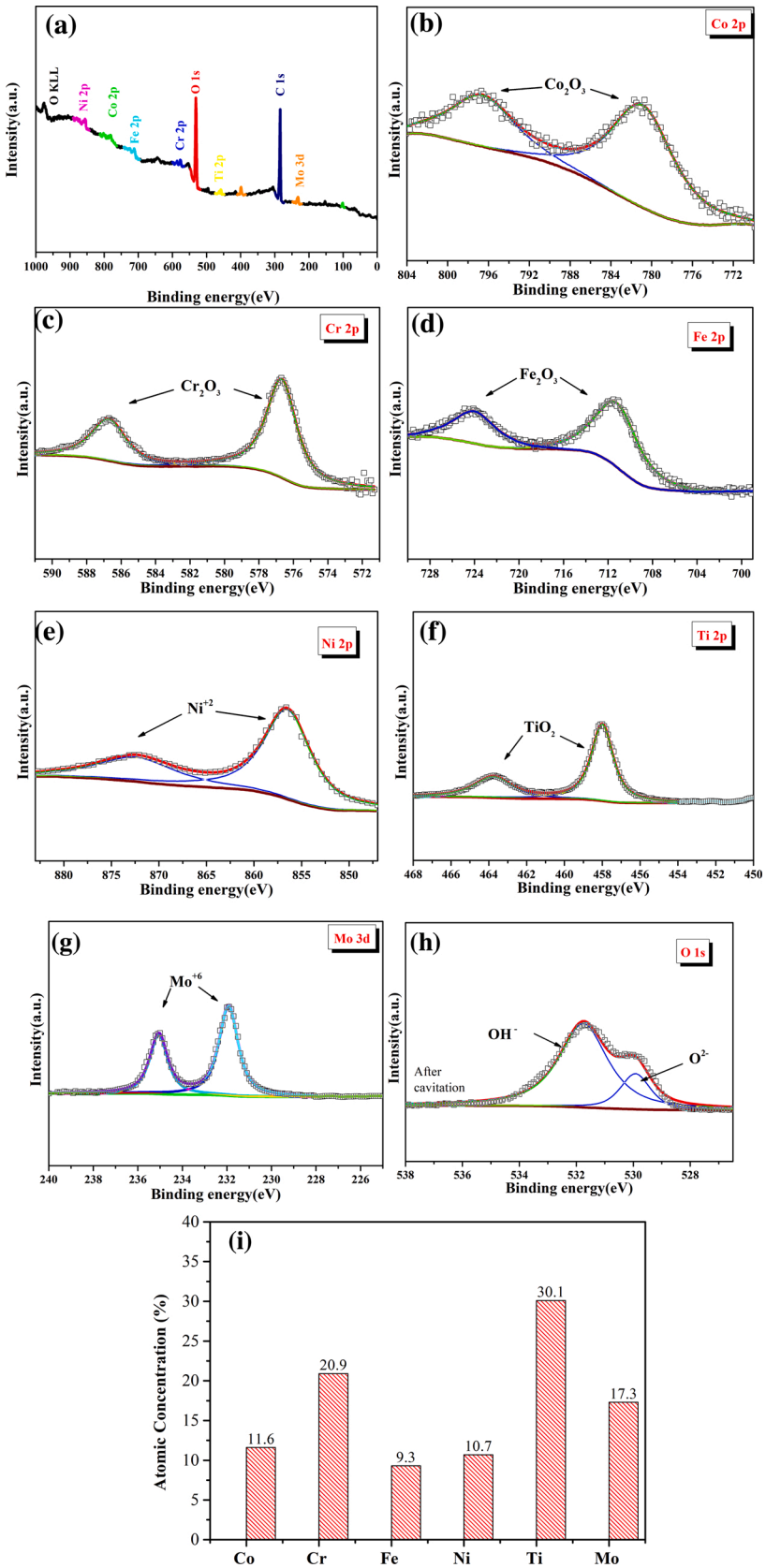

Fig. 12. XPS analysis was performed on the coating after 12 h of cavitation in 3.5wt% NaCl at output power of 800 W. (a) The XPS survey spectrum, (b-h) the high-resolution XPS spectra assigned to Co 2p, Cr2p, Fe 2p, Ni 2p, Ti 2p, Mo 3d and O 1s, respectively. (i) The content of the metal elements presents in the passive films on the HEA coating.

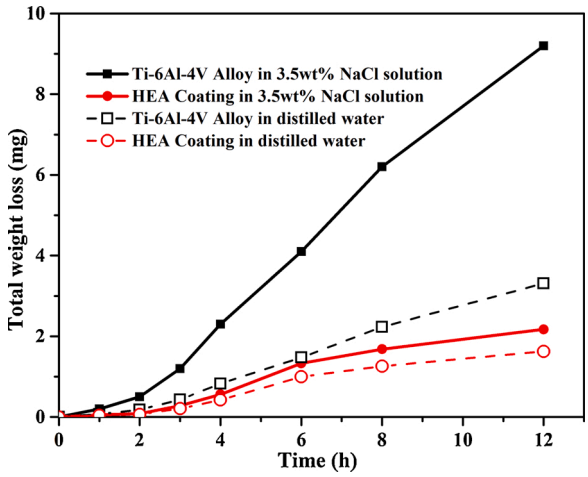

Fig. 13. The cumulative weight loss versus cavitation time curves for the HEA coating and uncoated Ti-6Al-4 V in 3.5 wt% NaCl and distilled water at output power of 800 W.

recorded signals correspond to their respective elemental metallic state [50–55]. Their concentrations are approximately equal consistent with the EDS analysis. From the XPS survey spectrum (Fig. 12 (a)), the observed peaks can be assigned to signals Co 2p, Cr 2p, Fe 2p, Ni 2p, Ti 2p, Mo 3d, O 1s and C 1s, respectively, and are apparently free of other metallic contamination. For the XPS Co 2p spectrum (Fig. 12(b)), two prominent peaks located at binding energies of 781.3 eV and 797.0 eV are observed, corresponding to the binding energies for Co $2p_{3/2}$ and Co $2p_{1/2}$, respectively, which agree well with the reported values for Co_2O_3 [50]. As shown in Fig. 12(c), the Cr 2p spectrum is composed of doublet peaks from Cr $2p_{3/2}$ and Cr $2p_{1/2}$ located at 576.7 eV and 586.7 eV, respectively, corresponding to the binding energy of Cr in stoichiometric Cr_2O_3 [51]. The XPS Fe 2p spectrum (Fig. 12(d)) consists of one doublet peak at 711.1 eV and 724.6 eV, assigned to Fe $2p_{3/2}$ and Fe $2p_{1/2}$, respectively. These binding energies are close to the literature data for Fe in Fe_2O_3 [52]. The XPS spectra of Ni $2p_{3/2}$ (Fig. 12(e)) and Ti $2p_{3/2}$ (Fig. 12(f)) located at 855.6 eV and 458.1 eV are assigned to the contributions of Ni^{2+} and Ti^{4+} oxidation states [53,54]. The Mo 3d spectrum (Fig.12(g)) consists of a doublet peak at 231.9 eV and 235.1 eV, respectively, corresponding to Mo $3d_{5/2}$ and Mo $3d_{3/2}$ peaks consistent with the Mo^{6+} oxidation state [55]. The asymmetric O1 s spectrum shown in Fig. 12(h) can be divided into two components: one peak at 529.9 eV corresponding to O^{2-} in oxides, and another one at 531.7 eV corresponding to the bound water or adsorbed OH^- ions from the surrounding environment [56]. As shown in Fig. 12(i), the oxide film formed on the HEA coating is enriched with Cr and Ti, which may be attributed to the preferential dissolution of other elements.

3.3.6. *Cumulative weight loss and eroded surface morphologies*

Fig. 13 shows the cumulative weight loss versus cavitation time curves for the HEA coating and uncoated Ti-6Al-4 V in both a 3.5 wt.% NaCl solution and distilled water at an output power of 800 W. During the first 3 h, the cavitation process for uncoated Ti-6Al-4 V is in an incubation stage, characterized by almost negligible amounts of weight loss, but subsequently enters a propagation stage with a sharp rise in weight loss under both media. On the contrary, the HEA coating exhibits a low slope of cumulative weight loss versus cavitation time in both media, and after 12 h of cavitation testing its cumulative weight loss is about four times lower than that of bare Ti-6Al-4 V. In this case, the cumulative weight loss of the tested samples in a 3.5 wt% NaCl solution represents the contribution of mechanical, corrosive and synergistic effects to the cavitation erosion damage, whereas the cumulative weight loss of the tested samples in distilled water is only attributed to mechanical erosion factor. Hence, the discrepancy in the cumulative weight loss between these two experimental conditions is assigned to corrosive and synergistic effects. As shown in Fig. 13, as the cavitation exposure time continues, the contribution of the pure mechanical erosion component to the total weight loss for bare Ti-6Al-4 V decreases, reflecting that both the corrosive and synergistic components play major roles in cavitation erosion of bare Ti-6Al-4 V with prolonged cavitation exposure time. In contrast, the contributions of the corrosive and synergistic components to the total weight loss for the HEA coating remain almost unchanged. Xie el at. [57] investigated the cavitation erosion behavior of $FeCoCrNiMo_XB_{0.2}$ HEA coatings prepared by laser cladding under the experimental conditions similar to those used in our case (including the tested solution and ultrasonic cavitation apparatus). The results showed that among three $FeCoCrNiMo_XB_{0.2}$ HEA coatings, the $FeCoCrNiMoB_{0.2}$ HEA coating exhibited the lowest cumulative weight loss of ~18 mg after cavitation periods of 6 h. Apparently, the biphasic CoCrFeNiTiMo coating reported here has a cumulative weight loss of 1.98 mg after the same cavitation time, implying that the coating possesses higher cavitation erosion resistance than these $FeCoCrNiMo_XB_{0.2}$ HEA coatings.

The changes in the eroded surface topography for the HEA coating and uncoated Ti-6Al-4 V substrate after cavitation erosion testing for different exposure times in a 3.5 wt% NaCl solution are shown in Fig. 14. As shown in Fig. 14 (a) and (b), after 1 h of cavitation testing, both the HEA coated and uncoated alloy exhibit relatively smooth surfaces, since plastic deformation of the surfaces is negligible during the incubation stage. This is consistent with the large capacitive semicircles in Nyquist plots for both samples as well as the low corrosion current density in the potentiodynamic polarization plots, suggesting that passive protective films had formed on their surfaces that act as a barrier to the charge transfer in this stage. After cavitation testing for 4 h (shown in Fig. 14(c) and (d)), some small craters and pits were observed on the surfaces of the uncoated Ti-6Al-4 V substrate, but the original surface machining marks are clearly visible for the HEA coating, together with a small number of small craters. After a further increase in cavitation exposure time (Fig. 14(e) and (g)), the appearance of the uncoated Ti-6Al-4 V alloy becomes rougher with a large number of microvoids and microcraters that are uniformly distributed over the substrate surface. This rough and porous surface further intensifies the corrosion degradation of uncoated Ti-6Al-4 V under cavitation erosion conditions due to the increased surface area. Furthermore, the surface cavitation destruction caused by the impacts of bubbles leads to stress accumulation on the surface and the formation of strain difference cells, where the potential in the stress-free areas is more positive than the stress-bearing areas. Note that the porous surface appearance of uncoated Ti-6Al-4 V after 8 h and 12 h of cavitation testing is consistent with the results predicted by the proposed EEC model. Therefore, in both cases, the corrosion degradation is exacerbated by the cavitation-corrosion process, evidenced by the significant increase of corrosion current densities and the decrease in charge transfer resistance. Simultaneously, the presence of Warburg impedance also confirms that that diffusion processes play an important role in the cavitation erosion for bare Ti-6Al-4 V. As shown in Fig. 14 (f) and (h), after 8 h and 12 h of cavitation exposure time, most areas of the HEA coating surfaces remain smooth and intact, with only a few, relatively small craters, which are responsible for the decrease in the overall cavitation erosion resistance. Wu et al. [58] suggested that hard, and uniformly distributed, intermetallic phases (such as Ti_2Ni and NiAl) enhanced the cavitation erosion resistance of $FeCoCrAlNiTi_x$ HEA coatings in distilled water. However, these intermetallic phases adversely affected the cavitation erosion resistance of these coatings in a 3.5 % NaCl solution, because these intermetallic compounds, can behave as cathodic sites, caused micro cell corrosion, thereby enhancing the synergistic effects between mechanical erosion and electrochemical corrosion attacks. As noted above, the Co_2Mo_3 phase distributed in the HEA coating improves mechanical parameters, such as hardness, H/E ratio and elastoplasticity. As a strengthening secondary phase, the Co_2Mo_3 phase increases the resistance of the HEA coating to the impact

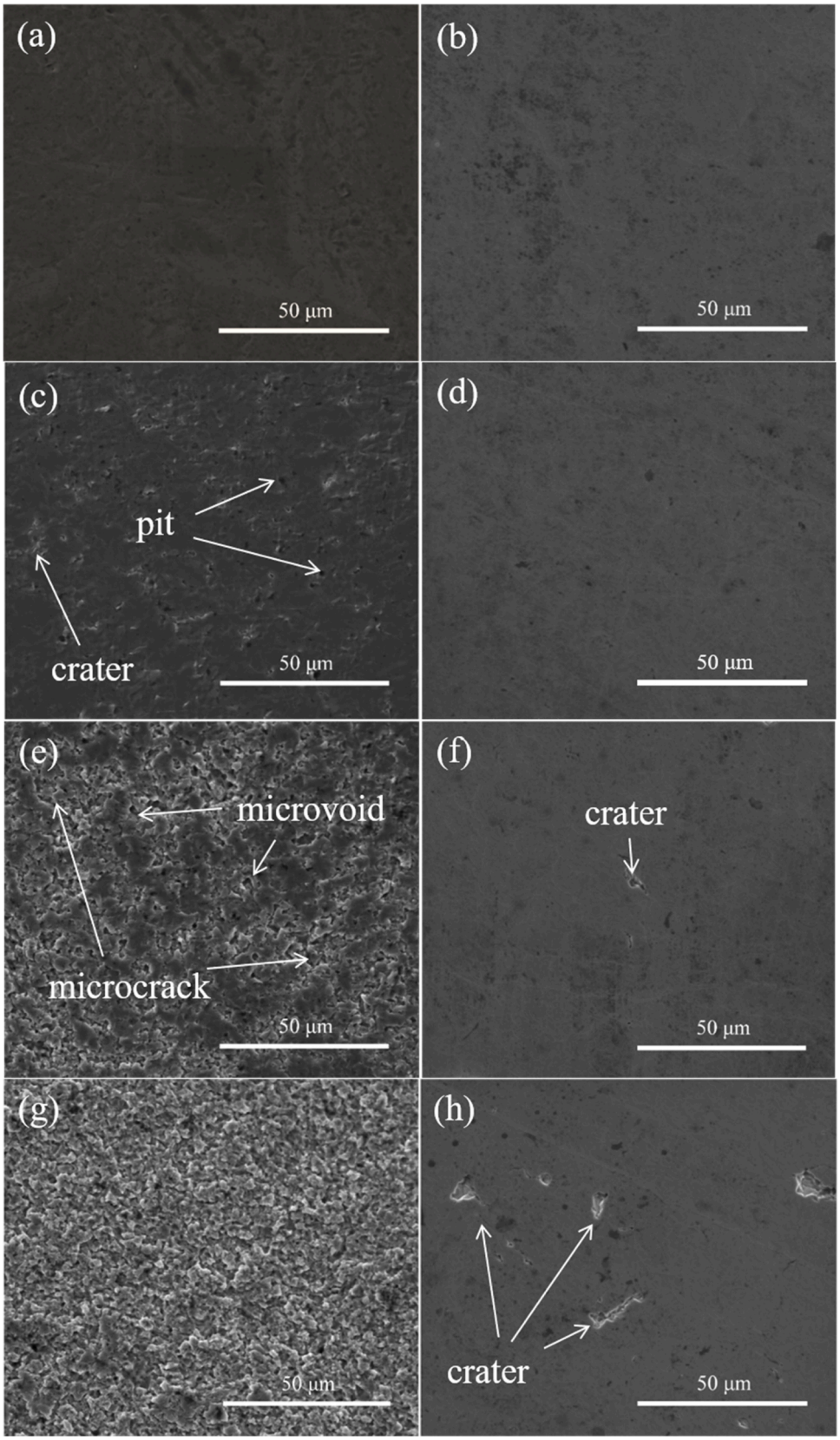

Fig. 14. The SEM images for eroded surface topography of (a, c, e and g) the uncoated Ti-6Al-4 V and (b, d, f and h) the HEA coating after cavitation erosion testing for the exposure time of (a and b) 1 h, (c and d) 4 h, (e and f) 8 h and (g and h) 12 h in 3.5 wt% NaCl solution.

stress that is generated by the collapsing bubbles by producing an anchoring effect on BCC-type solid solution phase to obstruct the nucleation and propagation of cracks [59]. According to the results of XPS analysis, during the ultrasonic cavitation process, the passive film formed on the HEA coating consists of a mixture of Co,Cr,Fe,Ni,Ti and Mo oxides. As can be seen from the potentiodynamic polarization plots (Fig. 7), at a given cavitation time, the current densities in the passive regions in the anodic branches for the HEA coating are markedly lower than those for uncoated Ti-6Al-4 V, suggesting that the mixed oxides grown on the coating have afford higher protection and stability than the oxide films present on uncoated Ti-6Al-4 V. The compact and stable oxides reduce the electrochemical corrosion attacks induced by Cl^- ions as the aggressive agent and the oxygen bubbles as the oxidation agent. Therefore, owing to its unique combination of good mechanical properties and high corrosion resistance, the HEA coating has a higher resistance to ultrasonic cavitation erosion in a 3.5 wt% NaCl solution in comparison to Ti-6Al-4 V.

4. Conclusions

A CoCrFeNiTiMo HEA coating was deposited onto a Ti-6Al-4 V substrate by a double cathode glow discharge technique. The phase composition, microstructure, microhardness, coating/substrate adhesion strength and cavitation erosion resistance in a 3.5 % NaCl solution have been investigated and the following conclusions can be drawn:

(1) The HEA coating consists of a body-centered cubic (BCC)-type solid solution phase and a tetragonal structured intermetallic Co_2Mo_3 phase. The as-prepared HEA coating comprises a ~ 10 μm thick deposition layer and a diffusion layer with a thickness of ~ 2 μm. The Co_2Mo_3 phase exhibits a strip like morphology and is uniformly distributed in HEA matrix.
(2) Nanoindentation tests indicate that the presence of Co_2Mo_3 phase increases hardness, H/E ratio and η value of the HEA coating. Scratch and Vickers indentation tests indicate that the HEA coating has a high load bearing capacity and a high threshold values for crack formation, which provides sufficient resistance to abrasion damage for applications involving heavy load conditions.
(3) Current-time responses and open circuit potential measurements indicate that the passive film developed on the HEA coating is more resilient and protective than that formed on uncoated Ti-6Al-4 V alloy, which exhibits less sensitivity to the cavitation erosion in aqueous corrosive environments.
(4) Potentiodynamic polarization measurements indicate that ultrasonic cavitation erosion renders the samples surface more electrochemically active and stimulates both anodic and cathodic reactions, and at a given cavitation time, the HEA coating exhibits a lower i_{corr} and more positive E_{corr} than uncoated Ti-6Al-4 V.
(5) The EIS measurements indicate that the resistance values of both the coating and bare Ti-6Al-4 V decreased with increasing of cavitation time, and for a given cavitation time, the resistance value for the HEA coating is about an order of magnitude higher than that for bare Ti-6Al-4 V. Moreover, PZC measurements demonstrate that the HEA coating has a stronger resistance to the absorption of chloride ions.

Declaration of Competing Interest

The authors declare that they have no known competing financial interests or personal relationships that could have appeared to influence the work reported in this paper.

Acknowledgements

The authors wish to acknowledge the National Natural Science Foundation of China for its financial support under projects of Nos. 52075245 and 51635004.

References

[1] Z. Cai, Y. Wang, X. Cui, G. Jin, Y. Li, Z. Liu, M. Dong, Design and microstructure characterization of FeCoNiAlCu high-entropy alloy coating by plasma cladding: in comparison with thermodynamic calculation, Surf. Coat. Technol. 330 (2017) 163–169.
[2] X.R. Wang, Z.Q. Wang, P. He, T.S. Lin, Y. Shi, Microstructure and wear properties of CuNiSiTiZr high-entropy alloy coatings on TC11 titanium alloy produced by electrospark — computer numerical control deposition process, Surf. Coat. Technol. 283 (2015) 156–161.
[3] H. Zhang, Y. Pan, Y. He, H. Jiao, Microstructure and properties of 6FeNiCoSiCrAlTi high-entropy alloy coating prepared by laser cladding, Appl. Surf. Sci. 257 (2011) 2259–2263.
[4] H.P. Chou, Y.S. Chang, S.K. Chen, J.W. Yeh, Microstructure, thermophysical and electrical properties in $Al_xCoCrFeNi$ ($0 \le x \le 2$) high-entropy alloys, Mater. Sci. Eng. B 163 (2009) 184–189.
[5] B.Y. Li, K. Peng, A.P. Hu, L.P. Zhou, J.J. Zhu, D.Y. Li, Structure and properties of $FeCoNiCrCu_{0.5}Al_x$ high-entropy alloy, Trans. Nonferrous Met. Soc. China 23 (2013) 735–741.
[6] W. Li, P. Liu, P.K. Liaw, Microstructures and properties of high-entropy alloy films and coatings: a review, Mater. Res. Lett. 6 (2018) 199–229.
[7] D.B. Miracle, O.N. Senkov, A critical review of high entropy alloys and related concepts, Acta Mater. 122 (2017) 448–511.
[8] D. Chen, F. He, B. Han, Q. Wu, Y. Tong, Y. Zhao, Z. Wang, J. Wang, J.-j. Kai, Synergistic effect of Ti and Al on $L1_2$-phase design in CoCrFeNi-based high entropy alloys, Intermetallics 110 (2019), 106476.
[9] G.A. Salishchev, M.A. Tikhonovsky, D.G. Shaysultanov, N.D. Stepanov, A. V. Kuznetsov, I.V. Kolodiy, A.S. Tortika, O.N. Senkov, Effect of Mn and V on structure and mechanical properties of high-entropy alloys based on CoCrFeNi system, J. Alloys. Compd. 591 (2014) 11–21.
[10] M.A. Avila-Rubio, J.A. Baldenebro-Lopez, R. Soto-Rojo, L.G. Ceballos-Mendivil, G. Carreño, N.F. Garza-Montes-de-Oca, F.J. Baldenebro-Lopez, Effect of Mo and Ti on the microstructure and microhardness in AlCoFeNiMoTi high entropy alloys prepared by mechanical alloying and conventional sintering, Adv. Powder Technol. 31 (2020) 1693–1701.
[11] Z. Guo, A. Zhang, J. Han, J. Meng, Microstructure, mechanical and tribological properties of CoCrFeNiMn high entropy alloy matrix composites with addition of Cr_3C_2, Tribol. Int. 151 (2020), 106436.
[12] S. Lavigne, F. Pougoum, S. Savoie, L. Martinu, J.E. Klemberg-Sapieha, R. Schulz, Cavitation erosion behavior of HVOF CaviTec coatings, Wear 386-387 (2017) 90–98.
[13] T. Amann, M. Waidele, A. Kailer, Analysis of mechanical and chemical mechanisms on cavitation erosion-corrosion of steels in salt water using electrochemical methods, Tribol. Int. 124 (2018) 238–246.
[14] H.R. Bakhshandeh, S.R. Allahkaram, A.H. Zabihi, An investigation on cavitation-corrosion behavior of Ni/β-SiC nanocomposite coatings under ultrasonic field, Ultrason. Sonochem. 56 (2019) 229–239.
[15] C.H. Tang, F.T. Cheng, H.C. Man, Laser surface alloying of a marine propeller bronze using aluminium powder, Surf. Coat. Technol. 200 (2006) 2602–2609.
[16] S.A. Saadi, Y. Yi, P. Cho, C. Jang, P. Beeley, Passivity breakdown of 316L stainless steel during potentiodynamic polarization in NaCl solution, Corros. Sci. 111 (2016) 720–727.
[17] J. Basumatary, R.J.K. Wood, Different methods of measuring synergy between cavitation erosion and corrosion for nickel aluminium bronze in 3.5% NaCl solution, Tribol. Int. 147 (2017), 104843.
[18] J. Xu, W. Liu, S. Jiang, P. Munroe, Z.H. Xie, Enhancing the cavitation erosion resistance of $D8_m$-Ta_5Si_3 nanocrystalline coatings through Al alloying, Ultrason. Sonochem. 50 (2019) 138–156.
[19] J. Xu, S.K. Zhang, X.L. Lu, S. Jiang, P. Munroe, Z.-H. Xie, Effect of Al alloying on cavitation erosion behavior of $TaSi_2$ nanocrystalline coatings, Ultrason. Sonochem. 59 (2019), 104742.
[20] S. Zhang, C.L. Wu, C.H. Zhang, M. Guan, J.Z. Tan, Laser surface alloying of FeCoCrAlNi high-entropy alloy on 304 stainless steel to enhance corrosion and cavitation erosion resistance, Opt. Laser Technol. 84 (2016) 23–31.
[21] W.C. Oliver, G.M. Pharr, An improved technique for determining hardness and elastic modulus using load and displacement sensing indentation experiments, J. Mater. Res. 7 (1992) 1564–1583.
[22] F. Tian, L.K. Varga, N. Chen, J. Shen, L. Vitos, Empirical design of single phase high-entropy alloys with high hardness, Intermetallics 58 (2015) 1–6.
[23] X. Yang, Y. Zhang, Prediction of high-entropy stabilized solid-solution in multi-component alloys, Mater. Chem. Phys. 132 (2012) 233–238.
[24] S. Guo, C. Ng, J. Lu, C.T. Liu, Effect of valence electron concentration on stability of fcc or bcc phase in high entropy alloys, J. Appl. Phys. 109 (2011), 103505.
[25] A.K. Singh, N. Kumar, A. Dwivedi, A. Subramaniam, A geometrical parameter for the formation of disordered solid solutions in multi-component alloys, Intermetallics 53 (2014) 112–119.
[26] Y. Dong, Y. Lu, L. Jiang, T. Wang, T. Li, Effects of electro-negativity on the stability of topologically close-packed phase in high entropy alloys, Intermetallics 52 (2014) 105–109.
[27] A. Takeuchi, A. Inoue, Mixing enthalpy of liquid phase calculated by miedema's scheme and approximated with sub-regular solution model for assessing forming ability of amorphous and glassy alloys, Intermetallics 18 (2010) 1779–1789.

[28] A. Erdogan, K.M. Döleker, S. Zeytin, Effect of laser re-melting on electric current assistive sintered CoCrFeNiAl$_x$Ti$_y$ high entropy alloys: formation, micro-hardness and wear behaviors, Surf. Coat. Technol. 399 (2020), 126179.
[29] X. Wang, Y. Zhang, Microstructures and corrosion resistance properties of as-cast and homogenized AlFeNiCuCr high entropy alloy, Mater. Chem. Phys. 254 (2020), 123440.
[30] J. Cheng, D. Liu, X. Liang, Y. Chen, Evolution of microstructure and mechanical properties of in situ synthesized TiC–TiB$_2$/CoCrCuFeNi high entropy alloy coatings, Surf. Coat. Technol. 281 (2015) 109–116.
[31] A. Krella, The influence of TiN coatings properties on cavitation erosion resistance, Surf. Coat. Technol. 204 (2009) 263–270.
[32] Fda S. Severo, C.J. Scheuer, R.P. Cardoso, S.F. Brunatto, Cavitation erosion resistance enhancement of martensitic stainless steel via low-temperature plasma carburizing, Wear 428-429 (2019) 162–166.
[33] M. E, H.X. Hu, X.M. Guo, Y.G. Zheng, Comparison of the cavitation erosion and slurry erosion behavior of cobalt-based and nickel-based coatings, Wear 428-429 (2019) 246–257.
[34] G. Hou, Y. Ren, X. Zhang, F. Dong, Y. An, X. Zhao, H. Zhou, J. Chen, Cavitation erosion mechanisms in Co-based coatings exposed to seawater, Ultrason. Sonochem. 60 (2020), 104799.
[35] A. Krella, A. Czyżniewski, Cavitation resistance of Cr–N coatings deposited on austenitic stainless steel at various temperatures, Wear 266 (2009) 800–809.
[36] J.G. Auret, O.F.R.A. Damm, G.J. Wright, F.P.A. Robinson, Influence of cathodic and anodic currents on cavitation Erosion, Corrosion 49 (1993) 910–920.
[37] L. Zhang, Y.K. Zhang, J.Z. Lu, F.Z. Dai, A.X. Feng, K.Y. Luo, J.S. Zhong, Q.W. Wang, M. Luo, H. Qi, Effects of laser shock processing on electrochemical corrosion resistance of ANSI 304 stainless steel weldments after cavitation erosion, Corros. Sci. 66 (2013) 5–13.
[38] S.-J. Kim, S.-J. Lee, S.-O. Chong, Electrochemical characteristics under cavitation-erosion for STS 316L in seawater, Mater. Res. Bull. 58 (2014) 244–247.
[39] M.S. Plesset, On cathodic protection in cavitation damage, J. Basic Eng. 82 (1960) 808–818.
[40] S. Hong, Y. Wu, J. Zhang, Y. Zheng, Y. Qin, J. Lin, Effect of ultrasonic cavitation erosion on corrosion behavior of high-velocity oxygen-fuel (HVOF) sprayed near-nanostructured WC-10Co-4Cr coating, Ultrason. Sonochem. 27 (2015) 374–378.
[41] Y. Zheng, S. Luo, W. Ke, Effect of passivity on electrochemical corrosion behavior of alloys during cavitation in aqueous solutions, Wear 262 (2007) 1308–1314.
[42] F. Bentiss, C. Jama, B. Mernari, H.E. Attari, L.E. Kadi, M. Lebrini, M. Traisnel, M. Lagrenée, Corrosion control of mild steel using 3,5-bis(4-methoxyphenyl)-4-amino-1,2,4-triazole in normal hydrochloric acid medium, Corros. Sci. 51 (2009) 1628–1635.
[43] R.K. Potucek, R.G. Rateick, V.I. Birss, Impedance characterization of anodic barrier Al oxide film beneath porous oxide layer, J. Electrochem. Soc. 153 (2006) B304–B310.
[44] C.H. Hsu, F. Mansfeld, Technical Note: concerning the conversion of the constant phase element parameter Y0 into a capacitance, Corrosion 57 (2001) 747–748.
[45] M.E. Orazem, P. Shukla, M.A. Membrino, Extension of the measurement model approach for deconvolution of underlying distributions for impedance measurements, Electrochim. Acta 47 (2002) 2027–2034.
[46] B. Hirschorn, M.E. Orazem, B. Tribollet, V. Vivier, I. Frateur, M. Musiani, Determination of effective capacitance and film thickness from constant-phase-element parameters, Electrochim. Acta 55 (2010) 6218–6227.
[47] P.S. Anjana, M.T. Sebastian, A.-K. Axelsson, N.M. Alford, Microwave dielectric properties of CeO$_2$–0.5AO–0.5TiO$_2$ (A=Ca, Mg, Zn, Mn, Co, Ni, W) ceramics, J. Eur. Ceram. Soc. 27 (2007) 3445–3452.
[48] N. Ibriş, J.C. Mirza Rosca, EIS study of Ti and its alloys in biological media, J. Electroanal. Chem. 526 (2002) 53–62.
[49] S. Gao, C. Dong, X. Cheng, K. Xiao, L. Wang, X. Li, Passive properties of magnetron-sputtered CrN film on AISI 304 stainless steel, Corrosion 70 (2014) 627–635.
[50] B.J. Tan, K.J. Klabunde, P.M.A. Sherwood, XPS studies of solvated metal atom dispersed catalysts. Evidence for layered cobalt-manganese particles on alumina and silica, J. Am. Chem. Soc. 113 (1991) 855–861.
[51] E. Desimoni, M. Cosimino, P.G. Zambonin, J.C. Rivière, An X-ray photoelectron spectroscopic study of some chromium-oxygen systems, Surf. Interface Anal. 13 (1988) 173–179.
[52] B.J. Tan, K.J. Klabunde, P.M.A. Sherwood, X-ray photoelectron spectroscopy studies of solvated metal atom dispersed catalysts. Monometallic iron and bimetallic iron-cobalt particles on alumina, Chem. Mater. 2 (1990) 186–191.
[53] G.C. Allen, P.M. Tucker, R.K. Wild, Surface oxidation of nickel metal as studied by X-Ray photoelectron spectroscopy, Oxid. Met. 13 (1979) 223–236.
[54] M.V. Kuznetsov, J.F. Zhuravlev, V.A. Gubanov, XPS analysis of adsorption of oxygen molecules on the surface of Ti and TiN$_x$ films in vacuum, J. Electron. Spectrosc. Relat. Phenom. 58 (1992) 169–176.
[55] C.R. Clayton, Y.C. Lu, A bipolar model of the passivity of stainless steel: the role of Mo addition, J. Electrochem. Soc. 133 (1986) 2465–2473.
[56] F.E. Castillejo, D.M. Marulanda, J.J. Olaya, J.E. Alfonso, Wear and corrosion resistance of niobium–chromium carbide coatings on AISI D2 produced through TRD, Surf. Coat. Technol. 254 (2014) 104–111.
[57] B.-q. Xie, Y.-f. Bao, C.-h. Zhong, Q.-n. Song, K. Yang, Y.-f. Jiang, Cavitation erosion resistance of high-entropy FeCoCrNiMo$_X$B$_{0.2}$ coatings cladded by laser, Surf. Eng. (2020), https://doi.org/10.1080/02670844.02672020.01846240.
[58] C.L. Wu, S. Zhang, C.H. Zhang, H. Zhang, S.Y. Dong, Phase evolution and cavitation erosion-corrosion behavior of FeCoCrAlNiTix high entropy alloy coatings on 304 stainless steel by laser surface alloying, J. Alloys. Compd. 698 (2017) 761–770.
[59] C.T. Kwok, F.T. Cheng, H.C. Man, Cavitation erosion and corrosion behaviors of laser-aluminized mild steel, Surf. Coat. Technol. 200 (2006) 3544–3552.